Green Chemistry

PAPER

View Article Online
View Journal | View Issue

Cite this: *Green Chem.*, 2025, **27**, 4205

Sustainable lithium recovery from geothermal brine *via* integrated membrane distillation – selective electrodialysis

Roviel Berhane Zegeye,[a] Ramato Ashu Tufa, *[a] Sergio Santoro, [a] Bruno Marco Inzillo,[a] Marco Aquino,[a] Grazia Giuseppina Politano,[a] Alula Selomon Embaye,[b] Pietro Argurio, [a] Loredana De Bartolo [b] and Efrem Curcio[a]

The escalating global demand for lithium, driven by its crucial role in energy storage systems and the transition to renewable energy, necessitates sustainable extraction methods from innovative sources such as geothermal brines, salt lakes and recycled batteries. Geothermal brine offers a dual advantage as a source of clean energy and lithium, with higher lithium concentrations (0.01–0.48 g L^{-1}) compared to seawater (0.18 mg L^{-1}) and levels comparable to salt lakes (0.04–3 g L^{-1}). Additionally, it features a much lower Mg/Li ratio (~35.33) compared to seawater (~7588), though still higher than that of salt lakes (~6.4). Despite these advantages, lithium recovery from geothermal brines is challenging due to low lithium concentrations and the presence of competing ions. Herein, we introduce a novel approach that integrates Membrane Distillation (MD) and Selective Electrodialysis (S-ED) for efficient lithium extraction and water recovery from geothermal brines. The focus is on optimizing performance at both stages: The MD process was optimized to reduce brine volume and specific thermal energy consumption, while the ED process was focused on minimizing voltage and specific energy consumption at the optimal concentration. The hybrid system demonstrates strong potential for energy-efficient lithium recovery. At MD stage, geothermal water was concentrated at different volume reduction factors (VRFs) of 15.1, 28.1 and 43.11, resulting in feed concentrations of 1 M, 2 M, and 3 M, respectively, for the subsequent ED stage. Operating the MD process with geothermal water at its natural temperature of 40 °C rendered it energy-neutral, leading to specific thermal energy savings of up to 1980.5 kW h m^{-3}. At S-ED stage, higher feed concentrations improved lithium selectivity but increased specific energy consumption. The optimal performance was observed at a feed concentration of 2 M (corresponding MD-VRF of 28.1) and an applied voltage of 2 V, achieving a specific energy consumption of 0.04 kW h per gram of Li^+ and a current efficiency of 4.1%. Overall, the integrated MD–S-ED approach demonstrates strong potential for energy-efficient lithium recovery, paving the way for innovative research and offering key insights for sustainable lithium extraction methods that support the principle of Circular Blue Economy and Green Process Intensification.

Received 27th December 2024,
Accepted 17th March 2025

DOI: 10.1039/d4gc06530a

rsc.li/greenchem

Green foundation

1. We present a pioneering integration of Membrane Distillation and Selective Electrodialysis for lithium recovery from geothermal brine, offering not only an energy-efficient and highly selective system but also one with significantly lower water footprints compared to conventional methods.
2. The integrated system's synergistic approach aligns with Green Process Intensification, enhancing water, energy, and resource recovery to drive the circular blue economy, while harnessing geothermal brines as both a clean energy source and a valuable lithium reservoir.
3. At the Membrane Distillation stage, membranes capable of operating at high brine concentrations with reduced concentration polarization and fouling (scaling) are essential, while the Selective Electrodialysis stage requires high-performing lithium-selective membranes.

[a]*Department of Environmental Engineering, DIAm, University of Calabria, Via Pietro Bucci CUBO 44/A, 87036 Rende, CS, Italy. E-mail: ramato.tufa@unical.it, rashtey@gmail.com*

[b]*Institute on Membrane Technology, National Research Council of Italy, ITM-CNR, Via Pietro Bucci CUBO 17/C, I-87036 Rende, CS, Italy*

1. Introduction

Lithium plays a crucial role in the advancement of the modern economy and high-tech industries, as well as for creating energy storage systems due its notable low density (0.534 g cm^{-3}) and high electrochemical standard potential (3.04 V).[1] It is recognized as being a strategic national resource widely used in lithium batteries, the ceramic industry, glass manufacturing, lubricants, and atomic thermonuclear fusion.[2–5] As global industrial development accelerates, the demand for lithium is sharply rising, driven by its importance in transitioning to cleaner energy sources.[6] Lithium can be sourced from three primary types of deposits: brines located in saline subsurface waters, clays altered by hydrothermal processes, and pegmatites, which are a form of crystalline igneous rock.[7–9] The majority of the world's lithium is found in the region known as the "lithium triangle", which encompasses salt lake areas in Chile, Argentina, and Bolivia, which holds over 50% of the global lithium resources and 60% of the reserves.[10] The increasing demand for critical raw materials utilized in emerging technologies and renewable energy systems poses significant challenges, particularly as many contemporary extraction processes are environmentally detrimental and deplete resources. Consequently, it is imperative to explore more sustainable mining resources such as geothermal brines and seawater, which can supply critical raw materials with reduced ecological impact.[11] These alternative sources not only help mitigate the environmental footprint of mining but also align with the principles of a circular economy and sustainability.[12–14] Lithium mining resources are currently the most abundant sources, but water resources have emerged as a promising alternative reservoir.[15–17] Some of these water resources containing lithium ions that can be potentially extracted include seawater, geothermal brines, oilfield brines, and groundwater. Geothermal brines not only contain substantial lithium reserves but also offer geothermal energy that can be harnessed concurrently.[18–20]

Geothermal brines, originating from within the earth, are saline solutions enriched with minerals due to their interaction with rocks. They hold significant promise as a dual source of clean energy and lithium.[21,22] Geothermal waters and oilfield brines are increasingly recognized as alternative sources of lithium, given their wide distribution and accessibility in various countries.[23] These sources provide essential local resources and support the business models of geothermal-energy projects through a zero-carbon emission targets. Lately, there has been a significant focus on the potential for utilizing non-traditional brines, such as deep groundwater brines and geothermal fluids.[24–26]

Recent developments in lithium recovery from geothermal brines highlight significant potential for further exploration. Sanjuan *et al.* found six lithium-rich geothermal sites located in Europe (Italy, Germany, France, and the United Kingdom) with Li^+ amounts varying from 125 to 480 mg L^{-1}.[27] In 2021, the EuGeLi (European Geothermal Lithium Brine) project produced the first kilograms of battery-grade lithium carbonate from geothermal waters in Alsace, located on the French-German border. Encouraged by the success of this project Eramet and Électricité de Strasbourg signed a memorandum of understanding to develop lithium production from geothermal brines in Rittershoffen (France), targeting 10 000 tons per year by 2030. Similarly, Vulcan Energy Resources released promising feasibility study results for lithium extraction in the Upper Rhine Valley.[28] Additionally, a study by Siekierka *et al.* utilized geothermal brine to extract lithium through the hybrid capacitive deionization method, resulting in lithium with a 73% concentration.[29] Several laboratory investigations validate the suitability of different techniques to extract lithium from geothermal brines and positive pilot results foster full commercialization.[30–32]

Despite the potential of geothermal brines, lithium recovery remains challenging due to the relatively low concentration of Li^+ and the presence of competing ions such as magnesium.[9,33] In this context, MD and its advanced variations provide promising approaches for brine dehydration, concentration, and Li recovery.[34] Additionally, the S-ED process effectively mitigates the interfering effects of Mg^{2+}, enhancing the efficiency of Li^+ recovery. In MD, water molecules evaporate from the heated aqueous feed solution (typically saline water), diffuse through a microporous hydrophobic membrane driven by a temperature-induced partial pressure gradient, and condense on the cooler permeate side, producing purified water.[35] MD's insensitivity to osmotic pressure permits sustained water recovery from saline solutions until supersaturation occurs, a stage termed Membrane Crystallization (MCr), where the crystallization of dissolved salts can be finely controlled.[36–38] In a novel fractionation method incorporating MCr, aimed at concentrating and purifying lithium brine, a water recovery of up to 95% was achieved while enriching lithium brines and purification.[39] MD in its photothermal variant, called Photothermal membrane distillation (PhMD), offers the advantage of enhanced distillation efficiency and minimizing the reliance on external energy sources for brine concentration and water recovery. This is achieved by integrating sunlight-absorbing materials that generate localized heat on the membrane surface.[40] A. H. Avci *et al.* showcased the effectiveness of photothermal membranes in Sweep Gas Membrane Distillation (SGMD) for concentrating synthetic seawater from 0.5 M NaCl to 4 M NaCl, producing hypersaline brine.[41] The use of photothermal membranes incorporating semiconductor photothermal flakes of WS2 in microporous hydrophobic membranes was also reported to increase the evaporation rates by up to 94% enabling the efficient extraction of lithium salts from concentrated brine.[42] Overall, MD/MCr or PhMD has proven to be a promising technology for efficient water recovery and lithium enrichment from various aqueous resources, including salt lake brines, offering an effective solution for the lithium dehydration and concentration step in lithium recovery processes.

S-ED is an emerging membrane-based process to separate lithium ions (Li^+) from magnesium ions (Mg^{2+}), a critical step

in lithium enrichment from brine lakes.[43] In S-ED, monovalent-selective cation- and anion-exchange membranes are arranged alternately between electrodes, channeling Li^+ into the concentrate stream while limiting Mg^{2+} passage. S-ED has been shown to efficiently lower the Mg/Li ratio to 2.07 and achieve lithium recovery rates above 90.5%, confirming its effectiveness for extracting lithium from salt lake brines with high Mg/Li ratios.[44,45] In a multi-stage S-ED process designed to treat simulated penetration water from a one-stage NF process, high-performance M-GA/PEI membranes at the S-ED stage successfully produced Li^+-rich solutions with high concentrations (8.33 g L^{-1}) and purity exceeding 96.4%.[46] Similarly, the S-ED process with M-Glu@PIP/PEI membranes was applied to treat simulated salt-lake brines (SLBs), demonstrating superior Li^+/Mg^{2+} separation performance and operational stability, achieving a Li^+ purity of 34.02%.[47] The primary advantage of S-ED in lithium recovery lies in the use of specialized monovalent selective membranes, which enable the efficient processing of complex lithium brine compositions while minimizing interference from competing ions, such as Mg^{2+}.

Combining the unique benefits of MD and S-ED for lithium recovery offers a synergistic approach in line with Process Intensification principles. This integration overcomes the challenges of standalone processes, providing a robust solution for promoting the circular Blue Economy and Green Process Intensification through optimized recovery of water, energy, and resources.[48–50] The implementation of the hybrid system enhances lithium extraction by concentrating the geothermal water, which simultaneously increases the lithium concentration and reduces the Mg/Li ratio. Moreover, using geothermal water in MD offers a sustainable solution for lithium extraction, leveraging the naturally elevated temperatures of 40 °C from geothermal sources to effectively reduce reliance on external heating, which cuts energy consumption and operational expenses. This innovative system enhances lithium recovery efficiency and promotes sustainability by utilizing renewable geothermal energy, while reducing water footprints associated with conventional evaporative technologies. Herein, we propose an innovative integrated MD–S-ED system for lithium extraction, particularly in enhancing the selectivity of magnesium–lithium (Mg/Li) separation, a critical challenge in lithium recovery from geothermal brines. We investigated the impact of feed concentration controlled by the volume reduction factor (VRF) in MD and voltage in S-ED on the efficiency of lithium recovery in the integrated MD–S-ED system. By optimizing these parameters, our objective is to enhance lithium selectivity and energy efficiency, achieving a more sustainable and effective process for simultaneous lithium extraction and water recovery from geothermal sources. To the best of our knowledge, this initiative represents the pioneering integration of MD and S-ED for lithium extraction from geothermal water, with the anticipation that our findings will contribute substantial insights and practical guidance for the future implementation of this combined technology.

2. Experimental

2.1. Materials and methods

2.1.1. Artificial solution. The feed stream consisted of a synthetic solution with initial composition based on real sample of geothermal water collected from Terme Luigiane in Guardia Piemontese (Italy) with natural temperature of 40 °C,[51] and treated with $NaHCO_3$ to remove Ca^{2+} ions by reactive precipitation. The synthetic solution was prepared dissolving lithium chloride (LiCl), sodium sulfate (Na_2SO_2), potassium chloride (KCl), magnesium sulfate heptahydrate ($MgSO_4{\cdot}7H_2O$), sodium bicarbonate ($NaHCO_3$) and sodium chloride (NaCl) in analytical grade (all purchased from Sigma-Aldrich SrL, Italy) in deionized water (5.5 μS m^{-1}) produced by PURELAB (Elga LabWater, UK) with the composition shown in Table 1.

2.1.2. Membrane distillation setup. MD tests were carried out in Direct Contact MD (DCMD) configuration using a Shell-and-Tube membrane module consisting of microporous polypropylene capillary membranes (Accurel PP S6/2), having pore size of 0.2 μm, porosity of 0.45, thickness of 50 μm, and a total membrane area of 0.1 m^2. Both feed (artificial geothermal water, tube side) and distillate (pure water, shell side) streams were continuously recirculated in counter-current mode by two Masterflex L/S digital peristaltic pumps (Cole-Parmer, US) at flowrate of 70 L h^{-1}. The feed temperature at the module inlet was maintained at 40 °C, simulating geothermal water conditions, using a CORIO CD heating immersion circulator (JULABO GmbH, Germany). The inlet temperature of the distillate was kept at 20 °C using a Digital Plus RTE201 thermostatic bath (Neslab, US). Temperature and pressure at the inlet and outlet of the shell and tube compartments were monitored using SPER SCIENTIFIC 800012 Pt multi-channel thermocouples with K-type probes (±0.1 °C resolution) and RF-D201 pressure gauges (DUNGS®, Germany), respectively. Transmembrane flux was calculated by measuring weight variations over time (±0.1 g resolution) using a REFLEX HP 8200 balance connected to the distillate tank.

2.1.3. Selective electrodialysis setup. S-ED tests were carried out in Micro ED stack provided by PCCell GmbH (Germany), containing monovalent cation exchange membranes (PC-MVK) and monovalent anion exchange membranes (PC-MVA) with an effective membrane area of 0.0006 m^2 and 5 cell pairs. Silicon/polypropylene spacers with thickness

Table 1 Ionic composition of initial geothermal water

Ions	Concentration (mg L^{-1}) Initial solution 0.07 M
Li^+	0.15×10^1
K^+	7.30×10^1
Mg^{2+}	5.30×10^1
Na^+	1.99×10^3
Cl^-	1.95×10^3
SO_4^{2-}	1.56×10^3

Table 2 Characteristics of ion exchange membranes used in the ED setup

Membrane type	Thickness (μm)	Ion exchange capacity (mequiv per g)	Chemical stability (pH)	Functional group	Resistance	Max. temperature (°C)
PC-MVK	100–120	Ca.1	0–10	Sulfonic acid	Ca. 6	45
PC-MVA	100–110	Ca.1	0–9	Ammonium	Ca. 5	60

0.45 mm, and electrodes made of inert Titanium with Pt/Ir coating as well as stainless steel were employed. The characteristics of the membranes used are presented in Table 2. A 0.5 M NaCl solution, mimicking seawater was used as a draw solution. The electrolyte solution was composed of 0.5 M Na_2SO_4. The feed, draw and electrolyte solutions were circulated through the stack compartments using Masterflex L/S digital peristaltic pumps (Cole-Palmer, US) at constant flow rates of 5 L h^{-1}. The temperature of the solutions was set by Digital plus RTE201 thermostatic baths (Neslab, US) and monitored by SPER SCIENTIFIC 800012Pt multi-channel thermocouples. The voltage-current characteristic of the ED was tested using an Autolab (Metrohm, US) in a galvanostatic mode by applying voltage in the range of 0 V to 5 V.

2.1.4. Hybrid membrane distillation-selective electrodialysis system. The conceptual scheme of the hybrid MD–S-ED is schematically depicted in Fig. 1. This integrated setup combines DCMD with S-ED to efficiently concentrate and recover valuable elements from synthetic geothermal waters. In the initial stage, DCMD was used to systematically concentrate the geothermal water by achieving several volume reduction factors, each corresponding to a total molar concentration. Three different brine solutions with concentrations of 1 M, 2 M and 3 M, obtained after the MD treatment of synthetic geothermal water samples, were used as the feed solution for the MicroED system. During S-ED tests, a DC voltage (from 1 to 4 V) was applied by RS PRO digital bench power supply (RS pro, UK). Samples from draw solution (100 mL) were taken every 30 min over a total run of 3 hours. This hybrid system was designed to operate in a continuous mode, ensuring a steady flow of concentrated brine from the DCMD stage directly into the S-ED stage. To evaluate long-term stability, the S-ED test was conducted for a 24 hour period under optimal conditions.

2.1.5. Atomic absorption spectroscopy analysis. Major ions (*i.e.* LI^+, Mg^{2+}, K^+ and Na^+) in the liquid samples were quantified by using a ContrAA 700 high-resolution continuum source atomic absorption spectrometer (HR-CS AAS) (Analytics Jena AG, Jena, Germany) with a high-intensity Xe short-arc lamp as continuum source, calibrated with ICP multi-element IV standard solution from Merck. Method parameters (*i.e.* fuel flow and burner height) were obtained by the flame automatic optimization procedure for the determination of the ions. The absorbance measurements were performed using the 670.78 nm, 285.21 nm, 766.49 nm and 589.00 nm spectral lines for the determination of LI^+, Mg^{2+}, K^+ and Na^+, respectively. The reproducibility of the determination of LI^+, Mg^{2+}, K^+ and Na^+, concentration was within ±5% range. Liquid samples were withdrawn and properly diluted with Milli-Q water (conductivity ≤0.055 μS cm^{-1}) to the calibration range of atomic absorption, *i.e.*, (0–3.5 mg L^{-1} for Mg), 0–0.5 mg L^{-1} for Li, K and Na and acidified with 1% v/v HNO_3. Since the precipi-

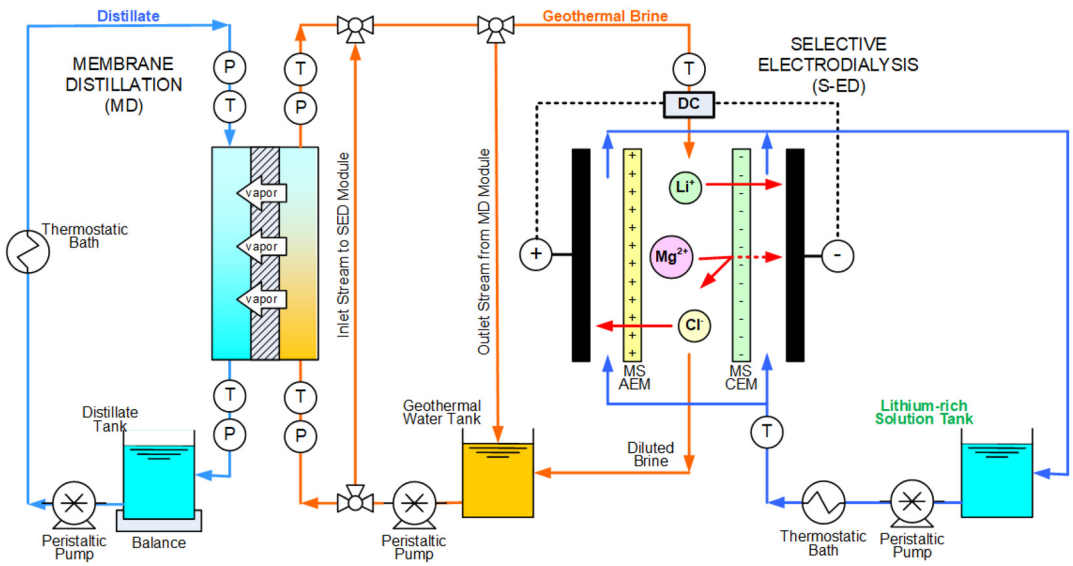

Fig. 1 Schematic representation of the conceptual lab-scale integration of DCMD and S-ED for simultaneous water and Li recovery from geothermal brine.

tation tests were performed under agitation, the stirring was stopped for 10 min before sampling to avoid the possible withdrawal of suspended precipitate in the liquid sample.

2.1.6. Data analysis. In this study, the main focus was on investigation of the impact of operating parameters such as voltage and concentration on the recovery of lithium ions in the product compartment, while limiting the migration of magnesium ions (Mg^{2+}) from the feed. To assess the S-ED separation effectiveness, the recovery rate of Li^+ (R_{Li}) and the leak rate of Mg^{2+} (L_{Mg}) were key metrics, which were quantified through the following eqn (1) and (2):

$$R_{Li} = \frac{\Delta[C_{Li,C} \times V_c]}{C_{Li,Di} \times V_{Di}} \times 100\% \quad (1)$$

$$L_{Mg} = \frac{\Delta[C_{Mg,C} \times V_c]}{C_{Mg,Di} \times V_{Di}} \times 100\% \quad (2)$$

where R (Li^+) is the recovery rate of Li^+, L (Mg^{2+}) is the leak rate of Mg^{2+}, $C_{i,c}$ is the concentration of the i^{th} ion in the concentrate stream, V_c is the volume of the concentrate solution, $C_{i,Di}$ is the initial concentration of the i^{th} ion in the feed solution, and V_{Di} is the initial volume of the feed solution. The selectivity of for lithium over magnesium ions was gauged using a metric known as Separation factor/selectivity ($S_{Li/Mg}$). This metric is calculated as the ratio of the transported lithium to magnesium ions, normalized by their respective initial mass ratios in the feed solution. The Mg/Li ratio ($X_{Mg/Li}$) was estimated from the ratio of the concentration of Magnesium to lithium ions in the concentrate stream as:

$$X_{Mg/Li} = \frac{C_{Mg,c}}{C_{Li,c}} \quad (3)$$

Additionally, this selectivity index is derived by taking the ratio of the lithium ion recovery rate (R_{Li}) to the magnesium ion leak rate L_{Mg}, used by Ball *et al.*[52] and is mathematically analogous to the "separation factor" in the context of nanofiltration.[53,54] It was calculated as:

$$S_{Li/Mg} = \frac{\left\{\frac{\Delta[C_{Li,c} \times V_c]}{\Delta[C_{Mg,c} \times V_c]}\right\}}{\left\{\frac{C_{Li,Di}}{C_{Mg,Di}}\right\}} = \frac{R_{Li}}{L_{Mg}} \quad (4)$$

The flux of ions in the concentrate compartment (J_i) was calculated as:

$$J_i = \frac{\Delta C_{i,C} \times V_c}{A \times \Delta t} \quad (5)$$

where A is the active membrane area. The current efficiency (η) is characterized as the proportion of the electrical charge that facilitates the movement of Li^+ ions compared to the total electrical charge delivered. This parameter was determined using the formula outlined in eqn (6):

$$\eta\,(\%) = \frac{(n_t - n_0) \times Z \times F}{N \int_0^t I(t)\mathrm{d}t} \times 100\% \quad (6)$$

where n_t is the number of moles of Li^+ in the concentrating compartment at time t, n_0 is the initial moles of Li^+ in the concentrating compartment, Z is the valence of Li^+, F is the Faraday constant (96 485 C mol^{-1}), N is the number of membrane pairs in the S-ED stack; and I and t refer to the current and the operating time, respectively. The specific energy consumption (E_{SEC}) quantifies the electrical energy required to recover one mole of lithium and serves as an essential factor for economic consideration. It was calculated using as follows:

$$E_{SEC} = \frac{U \int_0^t I(t)\mathrm{d}t}{n_r} \quad (7)$$

where U is the applied voltage, and n_r is the molar quantity of lithium ions that have increased in the concentrating compartment at the respective time t. The specific thermal energy consumption of the MD module ($STEC_{MD}$), measured in kW h m^{-3}, was determined by dividing the thermal energy supplied to the system by the distillate volume produced as follows:

$$STEC_{MD} = \frac{Q_f}{m_d} \quad (8)$$

where m_d is the distillate flow rate in m^3 h^{-1}, and Q_f is MD module thermal input in kW calculated by the following thermodynamic equation:

$$Q_f = m_f \times C_p \times (T_{f,in} - T_{f,out}) \quad (9)$$

where m_f is the feed flow rate in kg h^{-1}, C_p is the specific heat of the feed solution at constant pressure in kj kg^{-1}.K, $T_{f,in}$ and $T_{f,out}$ are the module feed inlet and outlet temperatures in K, respectively.

3. Results and discussion

3.1. Membrane distillation tests

Fig. 2 illustrates the variations of the transmembrane flux and geothermal brine concentration with concentration factor in DCMD experiments. The results demonstrate a clear correlation between transmembrane flux and the increasing concentration of geothermal water. The initial transmembrane flux in treating the geothermal brine (0.07 M) was 1.5 kg m^{-2} h^{-1}. At a concentration of 1 M, the transmembrane flux resulted of 1.2 kg m^{-2} h^{-1}, which suggests that lower feed concentrations typically result in higher flux rates due to the increased vapor pressure difference across the membrane.[55] In fact, higher solute concentrations lead to lower water vapor pressure, as described by Raoult's Law, which states that vapor pressure is proportional to the mole fraction of the solvent, with the activity coefficient also playing a role.[56] Accordingly, as the concentration increased to 2 M and then to 3 M, the transmembrane flux further decreased to 1.1 kg m^{-2} $h^{-1}$and 1.0 kg m^{-2} h^{-1}, respectively. This pronounced reduction in flux can also be attributed to the concentration polarization effect, which occurs when solute accumulation at the feed boundary layer reduces the effective vapor pressure, particularly at very high concentrations.[57] Despite this, the DCMD

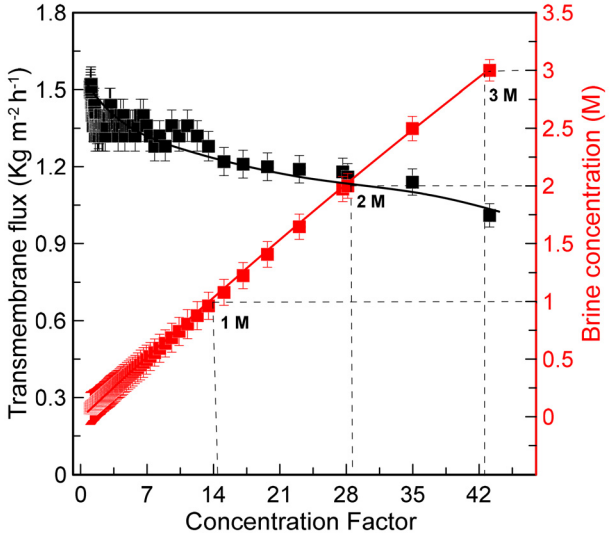

Fig. 2 DCMD treatment of geothermal water: the variation of transmembrane flux *versus* and brine (feed) concentration vs concentration factor.

process demonstrated high water recovery rates of 93.3%, 96.3%, and 97.6% for feed concentrations of 1 M, 2 M, and 3 M, respectively. The corresponding VRFs of 15.1, 28.1, and 43.1 highlight the efficiency of DCMD in concentrating geothermal water. These results validate the process's ability to operate effectively with minimal sensitivity to salinity of the retentate, an advantage that makes DCMD particularly suitable for concentrating brines. The specific thermal energy consumption at MD stage ($STEC_{MD}$) is a key parameter for assessing thermal energy efficiency. Higher voltages improved lithium recovery rates but compromised selectivity, as indicated by increasing Mg/Li ratios of the process. With an STECMD of roughly 2000 kW h m^{-3} based on eqn (8), the process is highly energy-intensive. While geothermal brine significantly reduces the reliance on additional thermal energy, temperature polarization remains a key limiting factor, as it leads to the formation of a thermal boundary layer that reduces the effective temperature gradient across the membrane. This, in turn, lowers vapor flux and decreases the thermal efficiency, ultimately affecting process scalability and energy sustainability.[58] To mitigate this effect, optimized module designs incorporating turbulence promoters and fluid-dynamic control strategies, including improved feed channel configurations and optimized flow conditions, can minimize temperature polarization by reducing boundary layer resistance and ensuring efficient heat distribution.[59–61] The integration of photothermal membranes represents another promising solution, as these materials convert incident light energy into localized heat at the membrane surface, increasing the driving force to mass transfer.[40] Other opportunities to mitigate $STEC_{MD}$ can be using renewable energy sources[62] or advanced photothermal nanomaterials.[63] However, geothermal brine offers the added advantage of being naturally heated, eliminating the need for anthropogenic thermal energy input. This makes geothermal brine an especially promising option for energy-efficient desalination and concentration processes. The substantial energy savings associated with geothermal brine further emphasize the potential for integrating geothermal energy into the MD process, particularly for resource recovery from geothermal brines.

The risk of membrane fouling in the MD stage was minimal in this study due to the naturally low calcium content of the geothermal brine used, eliminating concerns related to scaling from $CaCO_3$ or $CaSO_4$ precipitation. Furthermore, our group has previously developed an effective chemical precipitation method for calcium removal, ensuring that any residual Ca^{2+} in synthetic brines is eliminated before MD treatment. Drioli *et al.*[64] investigated calcium removal from nanofiltration (NF) retentate using a hollow-fiber gas–liquid membrane contactor, where CO_2 in NaOH generated HCO_3^- and CO_3^{2-} ions, leading to $CaCO_3$ precipitation and achieving a 56–89% reduction in Ca^{2+} depending on pH. Molinari *et al.* compared different Ca^{2+} precipitation strategies in seawater reverse osmosis (SWRO) brine, demonstrating that carbonate, hydrogen carbonate, and citrate ions effectively removed calcium, with carbonate precipitation significantly influenced by pH and leading to unintended $Mg(OH)_2$ formation at high pH (~12).[65] The stable transmembrane flux observed throughout the experiments confirms that the absence of Ca^{2+}, combined with proper pretreatment, effectively prevents scaling and ensures the optimal performance of the integrated MD–S-ED system.

3.2. Determination of limiting current density

One of the fundamental parameters in designing the ED process is the limiting current density (LCD).[66–69] The experimentally determined limiting current density (LCD) is commonly used to derive the critical boundary layer thickness in the process, with a direct proportionality to both the ion concentration and diffusivity.[67,69,70] Within the dilute channel boundary layer, the ionic concentration exhibits a sharp gradient, which becomes even more pronounced with an increase in applied current density.[71] To avoid water dissociation[67] and subsequent scaling of magnesium hydroxide,[66] it is essential to operate ED processes at a current density below the LCD. Exceeding a certain threshold in current density causes water molecules in the boundary layer to dissociate into H^+ and OH^- ions, leading to an undesirable increase in overall current density and a corresponding decrease in current efficiency.[68,72,73]

In our study, we systematically evaluated the Limiting Current Density (LCD) for different molar concentrations using cowan and brown method.[74] As shown in Fig. 3, for the 1 M solution, the LCD was 10.0 A m^{-2} at a voltage of 2.2 V, whereas for 2 M and 3 M solutions, the LCDs were 10.5 A m^{-2} and 11.1 A m^{-2}, with corresponding voltages of 2.1 V and 2 V, respectively.

Generally, the LCD increases with higher molar concentrations of the solution. For instance, as the molar concen-

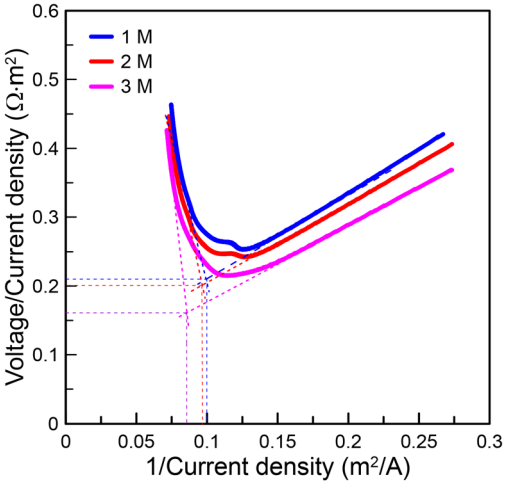

Fig. 3 LCD determination by cowan and brown method.

tration increases from 1 M to 3 M, about 11% increase in LCD is observed which indicates a positive correlation between ion concentration and LCD because higher ion concentrations enhance the mass transport of ions to the electrode surface, allowing for greater current flow before reaching the limiting threshold.[66,75–78] These findings guided us in establishing a voltage range between 1 and 4 V, encompassing a range close to the LCD, to investigate its impact on various performance parameters.

3.3. S-ED tests: impact of operating parameters

The performance of Li recovery in ED is influenced by several operating parameters, that have a direct impact on efficiency, selectivity, and energy consumption of the process. The applied electric potential and feed concentrations must be the carefully controlled to enhance the performance of Li recovery. The impact of variation on the ED voltage and feed concentrations was elucidated on key performance indicators – such as enrichment factor, ionic flux, SEC and current efficiency-were analysed using geothermal brines at three difference concentrations (1 M, 2 M and 3 M) and under four different electrical voltages (1 V, 2 V, 3 V and 4 V).

3.3.1. Effect of applied voltage. The efficacy of the micro ED system is significantly influenced by the applied voltage, which functions as the principal driving force for ion movement across membrane barriers, serving as the fundamental mechanism for ion transport. As shown in Fig. 4a, lithium recovery rates show a significant dependence on applied voltage, where increased voltage enhances the driving force for ion migration across IEMs. According to the Nernst–Planck equation, ion flux is governed by diffusion, migration, and convection. In the voltage range between 1 V and 3 V, Li^+ recovery increases gradually, from 4.5% to 5.7% for the 1 M solution and from 2.43% to 2.9% for the 3 M solution, following a regime in which ion migration remains proportional to the applied electric field. However, when the voltage is increased to 4 V, Li^+ recovery exhibits a more pronounced rise, reaching 10.7% for the 1 M solution and 4.19% for the 3 M solution. This phenomenon can be explained by the stronger electrostatic force acting on the ions, which enhances their migration across the membranes. The applied voltage at this stage slightly exceeds the limiting current density (LCD), increasing the driving force for Li^+ transport while reducing the resistance associated with ion movement. Additionally, the increase in Li^+ recovery at 4 V is accompanied by a decrease in selectivity, as evidenced by the increase in the Mg/Li ratio from 10.5 to 21.1. This suggests that the higher voltage reduces the charge-based discrimination of the membrane, facilitating the co-transport of Mg^{2+} and other competing ions. These results indicate that while operating at 4 V enhances lithium recovery, it also compromises selectivity due to the increased migration of interfering species. This trend is in agreement with observations in previous literature.[45,79–81] As to the concentration effect, the recovery rate decreased with increasing feed concentration, suggesting that higher solute concentrations might present different dynamics affecting ion mobility and membrane performance. Higher solute concentrations can lead to increased ionic strength, which affects the electrostatic interactions between the ions in the solution and the charged groups within the membrane matrix. These interactions can result in lower mobility for the ions due to increased resistance within the membrane matrix. The roughness in the electric potential causes a friction-like loss in the macroscale effective ion mobility, demonstrating how increased ionic strength and electrostatic interactions reduce ion mobility. Additionally, a thicker ion depletion layer forms beyond a diffusion-limited thickness, causing electroconvective instability. This instability reduces system performance by limiting ion diffusivity due to the highly depleted or accumulated ions on the membrane surface.[82–84] As a result, the lower recovery rates at higher concentrations, despite increased voltage, can be attributed to this decline in membrane performance, hindered by high ionic strength, which leads to reduced effective driving force for ion transport.

The Mg/Li ratio, initially at 35.53, varied significantly with applied voltage, impacting membrane selectivity. As illustrated in Fig. 4b, average Mg/Li ratios over 180 minutes were lower at the observed decrease in the Mg/Li ratio at 2 V compared to 1 V can be attributed to an optimized trade-off between selective ion transport and operating current density. At 2 V, the enhanced electrochemical driving force promotes the preferential migration of Li^+ while maintaining effective Donnan exclusion of Mg^{2+}. This effect results in a lower Mg/Li ratio compared to 1 V, where the electrochemical driving force is weaker, leading to less efficient lithium transport. Experimental data support this trend, showing that the average Mg/Li ratio at 1 V is 7.2, whereas at 2 V, it decreases to 6.5, confirming improved lithium selectivity. This behavior can be explained by the depletion of interfacial ion concentration at the membrane-solution interface, which strengthens the selective transport of monovalent ions under optimal current density conditions. The inherently higher mobility of Li^+ within the ion exchange membrane facilitates its preferential

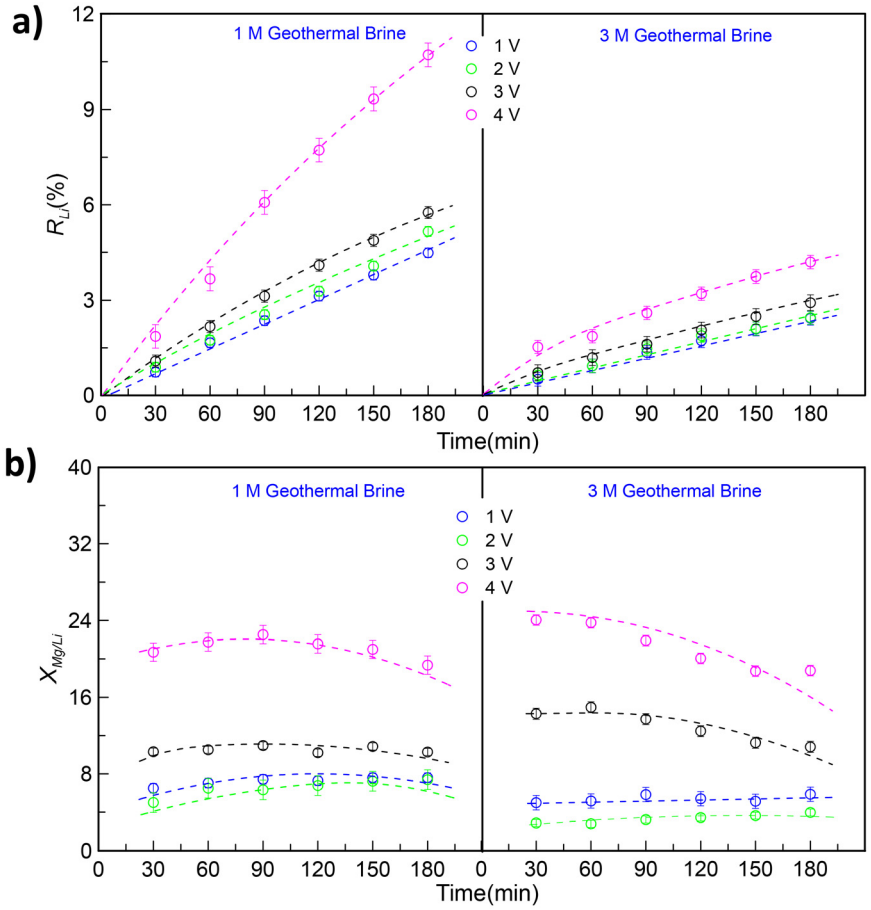

Fig. 4 Effect of applied voltage on (a) recovery rate of Li^+ at 1 M and 3 M; (b) Mg/Li ratio of concentrate stream *vs.* duration of time at 1 M and 3 M.

transport over Mg^{2+}, thereby reducing the Mg/Li ratio in the concentrate stream. However, as the voltage increases beyond 2 V, the Mg/Li ratio rises significantly, reaching 10.5 at 3 V and 21.1 at 4 V, indicating a decline in lithium selectivity due to the increased transport of Mg^{2+} at higher voltages. These findings are consistent with previous studies on selective electrodialysis for lithium–magnesium separation: Ji *et al.*[79] demonstrated that lithium migration increases with applied voltage, leading to an enhanced separation coefficient, while Nie *et al.*[44] found that higher current densities (up to 13.8 A m^{-2}) improve lithium selectivity by reducing the Mg/Li mass ratio in the product stream. Our results confirm that at 2 V, a balance is achieved between Li^+ recovery and Mg^{2+} exclusion, leading to an optimal Mg/Li ratio reduction. This trend was consistent across other concentrations, with the 3 M solution (Fig. 4b) showing ratios increasing from 5.3 at 1 V to 21.2 at 4 V, indicating reduced lithium selectivity. As voltage increases, the driving force for ion migration across the ion exchange membranes also increases, according to the Nernst–Planck equation which describes ion transport in response to both concentration gradients and electric fields.[85] This leads to an overall increase in ion flux; however, the selective transport of lithium ions does not necessarily increase proportionately. This loss of membrane selectivity under high voltage conditions shows that the increased energy can alter the interaction dynamics within the membrane pores, potentially allowing more interfering ions to pass through. Magnesium ions, having a different charge and possibly different interactions with the membrane material, may also be transported more efficiently at higher voltages. Additionally, when the applied voltage exceeds the LCD, the increased ion migration can lead to concentration polarization near the membrane surfaces[44,79,86] reducing the effective selectivity of the membrane by allowing a greater proportion of magnesium ions to migrate through. Moreover, Magnesium ions, being divalent, typically have a stronger hydration shell compared to monovalent lithium ions.[87] At lower voltages, the membrane might effectively discriminate against the larger hydrated magnesium ions, but as voltage increases, the energy provided might be sufficient to disrupt these hydration interactions, thus permitting more magnesium ions to permeate the membrane.[86,88,89]

Fig. 5 illustrates the effect of voltage on the separation factor ($S_{Li/Mg}$), which provide valuable insights into the selective efficacy of IEMs. These separation factors measure the relative concentration of lithium to magnesium in the product compared to the feed (eqn (5)). In general, the separation

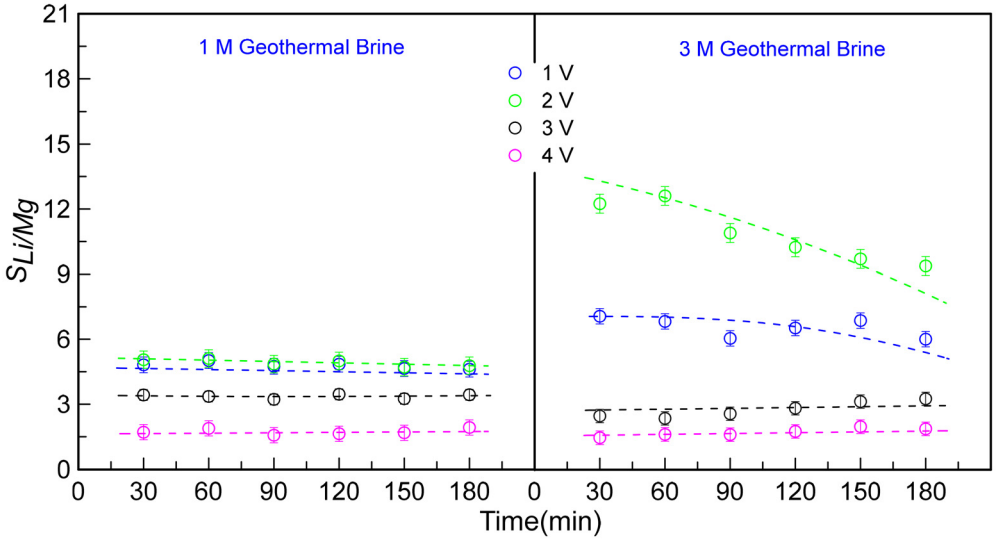

Fig. 5 Effect of applied voltage on separation factor of lithium and magnesium at 1 M and 3 M.

factor decreases as the applied voltage increases indicating a decrease in selective efficacy. As depicted in Fig. 5, for the 1 M solution, the separation factor factors over 180 minutes decreased from 4.6 at 1 V to 1.9 at 4 V. The diminished membrane selectivity as the voltage increased is in line with the increasing Mg/Li ratios observed at higher voltages, such as 3 V and 4 V, where the ratios increased from 10.5 to 21.1, respectively. This also suggests increased co-transport of magnesium ions alongside lithium ions through the membrane in line with the depleted membrane selectivity. It's worth also noting that higher voltages (3 V and 4 V) exceed the LCD, negatively impacting membrane selectivity. Under higher applied current densities, the ionic concentration gradient in the dilute channel boundary layer becomes steeper, which can lead to concentration polarization and a decrease in membrane selectivity.[71] As discussed earlier, higher voltages also drive faster migration of Mg^{2+} which would lead to poor separation result.[90] For 3 M geothermal brine, the separation factor increased with the increasing voltage as well (Fig. 5). For both the 1 M and 3 M feed solutions, the highest separation factor of 4.7 and 9.3 (at 180 min), respectively, were achieved at 2 V, indicating optimal selectivity at this voltage. The results demonstrate that the optimization of the electrochemical driving force at 2 V enhances Li^+ ion transport over Mg^{2+} ions and significantly improves selectivity at high current densities near LCD, underscoring the importance of applied voltage in S-ED performance.

As illustrated in Fig. 6a, the concentrations of migrated Li^+ in the receiving solutions increase linearly with voltage for both solutions, indicating that higher applied voltages result in higher fluxes. At 1 V in the 1 M solution, the process achieved an average ion flux of 0.13 mmol m^{-2} min^{-1}, which increased to 0.32 mmol m^{-2} min^{-1} at 4 V. Similarly, in the 3 M solution, the ion flux was 0.2 mmol m^{-2} min^{-1} at 1 V and rose to 0.36 mmol m^{-2} min^{-1} at 4 V. This increase results from the enhanced electric field, which strengthens ion electromigration and facilitates ion transport across the membranes in S-ED. The observed trend confirms that ion flux is primarily governed by the applied voltage and the associated migration effects. According to Ohm's law, electric voltage is directly proportional to electric current; thus, higher voltage results in greater electric current flowing from the anode to the cathode.[91] Moreover, as depicted in Fig. 6b, the migration of Mg^{2+} at 1 V in the 1 M solution shows an increase in ion flux from 0.28 to 1.61 mmol m^{-2} min^{-1} at 4 V, while in the 3 M solution, the ion flux increased from 0.33 mmol m^{-2} min^{-1} at 1 V to 1.93 mmol m^{-2} min^{-1} at 4 V. This concurrent rise in Mg^{2+} flux at elevated voltages reflects a compromise, where the selectivity for Li^+ over Mg^{2+} decreases, highlighting the challenges in maintaining high selectivity under high-voltage conditions.

3.3.2. Effect of concentration. The hybrid MD–S-ED system's response to varying solute concentrations provides comprehensive data to examine the complex interactions impacting membrane performance parameters. The S-ED processes were conducted under the constant voltage of 2 V, which aligns with the LCD, to evaluate the effect of feed concentration on S-ED performance. Fig. 6c depicts recovery rate of lithium over time at 2 V for three different solution concentrations (1 M, 2 M, and 3 M) of different volume reduction factors from MD. The data indicates a linear increase in lithium recovery rate for all concentrations. Notably, the 1 M solution demonstrates the highest recovery rate, reaching 5.1% after 180 minutes. The 2 M solution follows with approximately 3.85%, while the 3 M solution has the lowest recovery rate, at 2.45% after the same duration. This phenomenon can be attributed to the increased ionic strength in the feed solution and the greater concentration gradient between the feed and product chambers. As the feed concentration rises, both cell conductivity and the number of transferred ions increase.

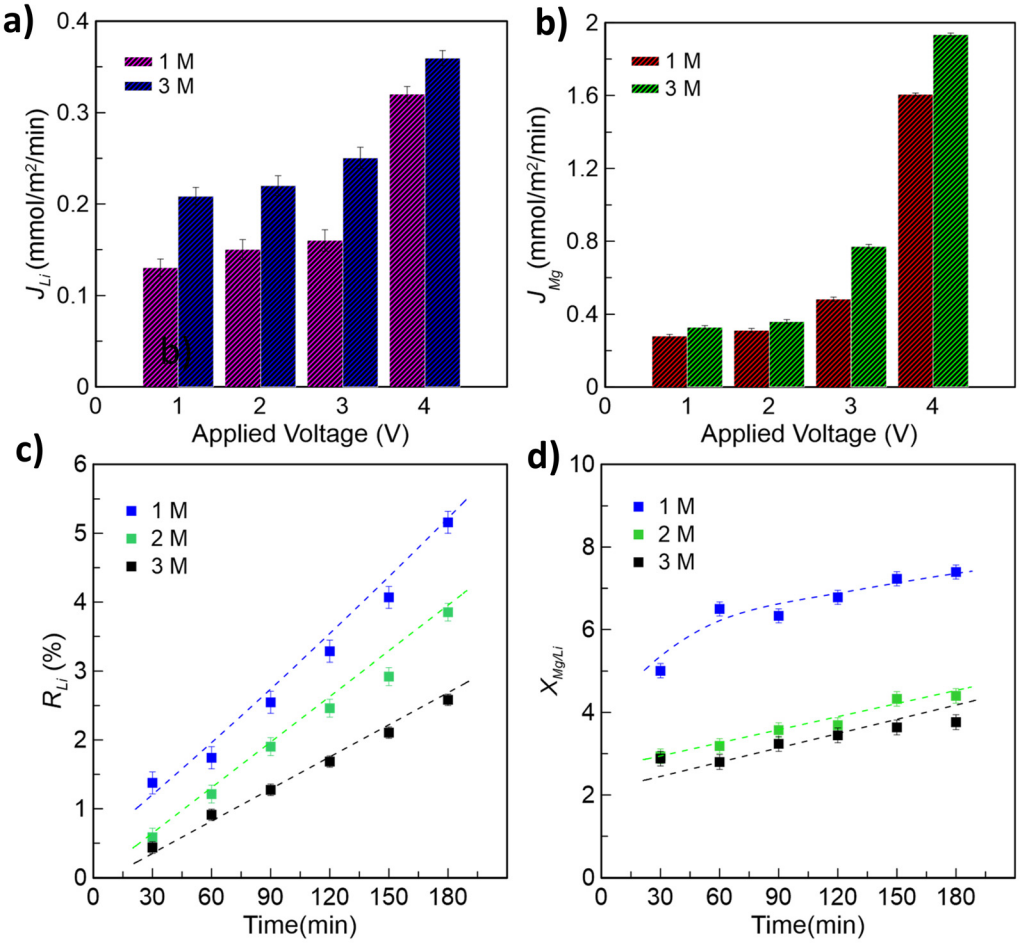

Fig. 6 Effect of applied voltage on the flux of lithium at (a) 1 M and 3 M, and magnesium at (b) 1M and (d) 3 M. Effect of different concentrations on (c) recovery rate of Li^+ and (d) Mg/Li ratio of concentrate stream. The applied voltage remains at 2 V in all cases.

However, the membrane's capacity to transport ions is limited, ultimately leading to a decrease in lithium recovery rates at higher concentrations. Despite the higher number of lithium ions transferred with increased initial feed concentration, the overall recovery decreased due to the initially high lithium ion count in the feed solution which is in agreement with literature.[89,92,93] The effect of feed concentration at constant voltage on selectivity is illustrated by the Mg/Li ratio, as shown in Fig. 6d. The data indicates higher selectivity at 3 M, with an Mg/Li ratio of 3.96, compared to lower selectivity at 1 M, with an Mg/Li ratio of 7.3. This shows that at higher feed concentrations at a constant voltage below LCD, the selectivity of the membrane for lithium ions improved. This is likely because, in S-ED, operating at higher current densities to 70% of the LCD benefits the recovery ratio. It has been reported that higher current densities can enhance counterion selectivity across various resource recovery applications.[94–98]

In the present study, the current density was maintained near the LCD value. At increased current densities, the ion concentration at the membrane–solution interface depletes further due to the limitations in ion diffusion across the boundary layer.[96,99] This depletion results in a dilutive effect that enhances counterion selectivity through Donnan exclusion, thereby increasing the ion migration. The enhanced Donnan exclusion of Mg^{2+} is further magnified by the inherently higher mobility of monovalent cations within the CEM, leading to a more significant increase in the apparent monovalent selectivity factors.[100]

3.3.3. Permeation performance of coexisting cations. In the integrated MD–S-ED process, the presence of high concentrations of Na^+ and K^+ ions poses significant challenges on the recovery of Li^+ from geothermal brine due to ion migration alongside Li^+. To better understand this phenomenon, the permeation sequence of Na^+, K^+, lithium Li^+, and Mg^{2+} ions was evaluated under a constant voltage of 2 V across varying molar concentrations. As illustrated in Fig. 7a, distinct permeation sequence was observed: $Na^+ > K^+ > Li^+ > Mg^{2+}$. Sodium ions showed the highest recovery rates across all tested conditions. The high permeation of Na^+ is attributed to its smaller hydrated radius (0.358 nm) and lower hydration energy (-406 kJ mol^{-1}), which enhance its interaction with the membrane. Additionally, the high concentration of Na^+ in the brine

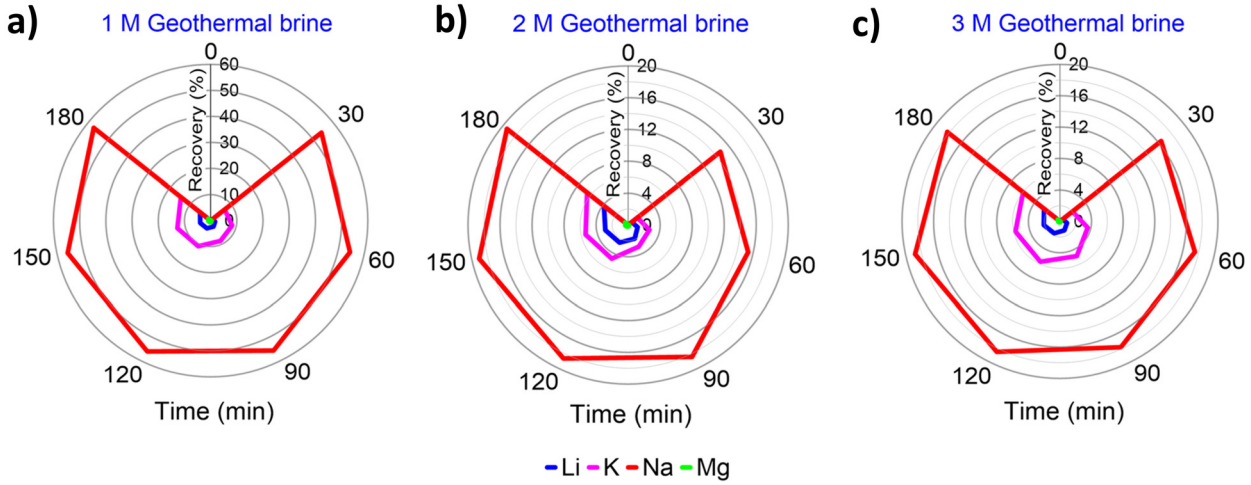

Fig. 7 Cation permeation sequence for (a) 1 M solution, (b) 2 M solution, and (c) 3 M solution at an applied voltage of 2 V.

increases its competitive advantage, leading to substantial migration through the membrane. In 1 M solutions, Na^+ achieved a recovery rate of 57.08% after 180 minutes, while in 2 M and 3 M solutions, the recovery rates dropped to 18.61% and 18.23%, respectively. This decline in recovery rates at higher concentrations can be attributed to increased ion-ion interactions and steric hindrance, which limit the mobility of Na^+ ions as their concentration rises.[101] K^+ ions exhibited a similar but less pronounced trend, as shown in Fig. 7a. In 1 M solutions, K^+ recovery increased from 6.85% at 30 minutes to 14.53% after 180 minutes. At higher molarities, K^+ recovery stabilized at lower values, with 6.55% in 2 M and 4.07% in 3 M solutions, as illustrated in Fig. 7b and c. Despite having a hydrated radius similar to sodium ions (0.331 nm) and a lower hydration energy (−322 kJ mol^{-1}), the lower concentration of K^+ compared to Na^+ reduces overall its performance efficiency. However, K^+ still permeates more effectively than Li^+ due to its moderate hydration energy, whereas Li^+, with a higher hydration energy (−520 kJ mol^{-1}), forms a stronger hydration shell that hinders its transport through the membrane. These characteristics make K^+ more competitive in the ion migration process relative to Li^+ under the tested conditions. Mg^{2+}, due to their divalent nature, exhibited the lowest permeation rates among all tested cations, highlighting the membrane's selectivity. Mg^{2+} recovery remained minimal, staying below 1.08% even after 180 minutes in 1 M solutions, with similar low recoveries observed at 0.48% and 0.28% in 2 M and 3 M solutions, respectively. Mg^{2+} has a much larger hydrated radius (0.428 nm) and significantly higher hydration energy (−1922 kJ mol^{-1}) due to its divalent charge. These characteristics result in strong electrostatic interactions and a robust hydration shell, which create substantial resistance to permeation through the monovalent selective membranes. Lithium ions, although monovalent, exhibited lower permeation rates compared to Na^+ and K^+. Li^+ has a smaller ionic radius but forms a very strong hydration shell, resulting in a larger effective hydrated radius (0.382 nm) and high hydration energy (−520 kJ mol^{-1}). These properties increase resistance to migration through the membrane's selective sites. The high charge density of Li^+ leads to strong interactions with surrounding water molecules, forming a stable hydration shell that impedes ion transport. These findings demonstrate that steric hindrance has played a significant role in the partitioning of the ionic species in the geothermal feed solution.

3.4. Current efficiency

Electrodialysis (ED) technology offers low capital expenses due to its compact membrane stack design. However, a significant factor in its feasibility is the operating costs. As an electro-driven process, ED requires energy to counteract ion diffusion resistance and the inherent resistance of both the solution and the membrane. Achieving high energy efficiency during ED operation is vital, as it plays a key role in determining the overall effectiveness of the process. Among various metrics, current efficiency stands out as a critical parameter for evaluating the operational efficiency of ED systems.[102] The current efficiency is defined as the ratio of the electric charge contributed to the transport of the valuable target ion (typically Li^+ in this study) to the total supplied electric charge. Average current efficiency at a lower voltage of 1 V for the 1 M solution was 12.9% over 180 minutes. However, as the voltage increased to 4 V, the system dynamics shifted significantly; despite achieving the highest lithium recovery rate, current efficiency reduced to 0.13%, as shown in Fig. 8a. This trend of diminishing returns with increased voltage was similarly observed in solutions with higher ionic strengths. As shown in Fig. 8a, the current efficiency drastically dropped from 9.95% at 1 V to 0.11% at 4 V for 3 M.

The reduction in current efficiency is primarily attributed to the higher concentration of lithium in the concentrate solution chamber, resulting from the increased voltage. At higher voltages, the supply of Li^+ ions from the diffusion boundary layer to the membrane surface becomes insufficient to replenish the transported ions. Consequently, secondary effects such

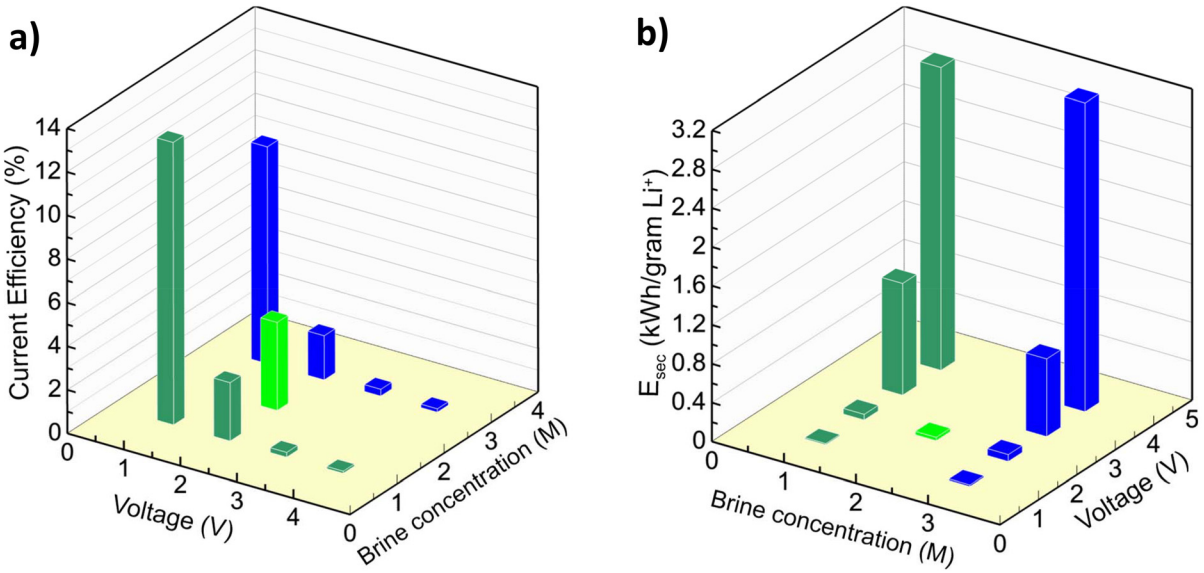

Fig. 8 (a) Average current efficiency at varying voltages for 1 M and 3 M concentrations, and at different concentrations (1 M, 2 M, and 3 M) at a constant voltage of 2 V. (b) Average specific energy consumption at varying voltages for 1 M and 3 M concentrations, and at different concentrations (1 M, 2 M, and 3 M) at a constant voltage of 2 V.

as concentration polarization and water splitting are amplified, contributing more to the current at higher current densities, thus reducing the effective electric current available for the transport of target ions.[44] Our results also follow a similar trend observed in the literature.[79,80] It can be concluded that the increase in voltage is beneficial to promote ion migration and thus increase the recovery ratio of lithium ions. The excessive voltage also promotes the leaky migration of other coexisting ions, thereby reducing the current efficiency of Li^+, which is not conducive to the recovery of Li^+. Over the course of 180 minutes, the average current efficiency declined from 2.65% for the 1 M solution to 2.36% for the 3 M solution at 2 V applied voltage. Notably, the 2 M solution demonstrated optimal performance metrics, achieving the highest current efficiency at 4.14% as shown in Fig. 8a.

3.5. Specific energy consumption

Specific energy consumption is a key parameter for evaluating ED performance, reflecting the energy required to recover one unit of ions. In this study, operating costs were assessed based on specific energy consumption, defined as the ratio of total electrical work to the mass of Li^+ ions transported. This metric was used to quantify the electric energy consumed per gram of lithium transported. Unlike current efficiency, SEC considers both current and voltage, providing a more comprehensive evaluation of the ED system's operational efficiency.[103] As shown in Fig. 8b, the average SEC at a lower voltage of 1 V for the 1 M solution was 0.013 kW h per g Li^+. However, as the voltage increased to 4 V, the SEC rose significantly to 3.11 kW h per g Li^+. Clearly, this effect was attributed to the increased energy required to transport coexisting ions at higher voltages. SEC increased when the voltage increased for higher molarities of solutions. As shown in Fig. 8b, the average SEC for the 3 M solution increased from 0.016 to 3.17 kW h per g Li^+. SEC is directly related to the electrical potential difference generated and the variations in electrical current over time, while it decreases with the increase in the number of moles removed from the feed compartment. Observations indicate that, with higher applied voltage, the impact of the increased electrical potential and the changes in electrical current over time surpass the counteracting effects of the increased number of moles removed from the feed compartment.[104] During the 180 minute period, the average SEC increased from 0.053 kW h per g Li^+ in the 1 M solution to 0.065kW h per g Li^+ in the 3 M solution at constant voltage of 2 V. The 2 M solution showed the best performance, with the lowest SEC recorded at 0.04 kW h per g Li^+ at 2 V applied voltage as shown in Fig. 8b.

Our results indicate that gains in monovalent selectivity at a higher current density below the LCD are accompanied by increase in SEC. This finding highlights a steep trade-off between ion selectivity and energy efficiency in geothermal brine lithium extraction, governed by the applied current density. Foo *et al.* observed comparable patterns in hypersaline salt-lake brines, where a 6.25-fold improvement in Li^+/Mg^{2+} selectivity was associated with a 71.6% rise in SEC when operating at high current density below LCD, attributable to inevitable entropy generation caused by Joule heating.[105] The optimal performance metrics observed at 2 M concentration can be attributed to a combination of reduced electrical resistance, minimized side reactions, enhanced Donnan exclusion, and the high mobility of lithium ions. The balanced ionic strength at 2 M enhances ion transport efficiency while preventing the membrane from being overwhelmed by excessive ionic competition or saturation effects.

In contrast, the 1 M solution, despite displaying moderate current efficiency, incurs higher SEC due to lower ionic strength and increased resistance, which hinder efficient ion transport. Conversely, the 3 M solution, although exhibiting high selectivity for lithium ions, suffers from significant ionic competition and membrane saturation, resulting in the highest SEC and the lowest current efficiency. These findings highlight the delicate balance required in ED processes: At high current density below the LCD, higher feed concentration can enhance selectivity *via* improved Donnan exclusion, but it also introduces inefficiencies due to increased ionic competition and saturation. Therefore, the 2 M solution stands out as the optimal concentration, achieving both low energy consumption and high current efficiency, underscoring its potential for more efficient and sustainable lithium recovery. Table 3 provides a comprehensive comparison of the selectivity index ($S_{LI/Mg}$) and SEC between our study and S-ED from previous studies. The $S_{Li/Mg}$ in this study ranged from 1 to 13, outperforming some S-ED studies such as,[89] which reported lower selectivity of 4.6. Furthermore, the Sec for MD–S-ED is significantly lower that of S-ED in most cases achieving better energy efficiency.

Table 3 Comparison of Selectivity and specific energy consumption of MD–S-ED with literature

Process	$S_{Li/Mg}$	SEC (kW h per g Li^+)
In this study	1–13	0.01–3.17
ED[53]	8–10	0.02
S-ED[86]	10–25	1–3
S-ED[89]	4.6	0.2
S-ED[106]	NA[a]	0.07–0.57
ED[107]	24.1–33.9	0.5
S-ED[108]	NA	0.76–0.99
S-ED[80]	14.7	0.012
S-ED[109]	4.82	NA
S-ED[105]	4–6	0.02–0.6
S-ED[110]	NA	0.0019–0.5
ED[90]	1–26	0.018
S-ED[111]	NA	0.02
S-ED[44]	20–33	0.0019
S-ED[45]	9.8	0.0045
S-ED[95]	NA	0.0056–0.12
ED[112]	5.27	NA
ED[113]	NA	0.02

[a] Not available.

Optimizing the synergy between MD and S-ED is essential for achieving efficient and selective lithium recovery. By leveraging geothermal heat (40 °C), the MD stage operates without external thermal energy input, significantly reducing STEC. The concentrated brine from MD is then fed into the S-ED stage, where lithium is selectively recovered under optimized conditions. Maintaining VRF of 28.1 in MD (corresponding to a 2 M lithium concentration) and applying an optimal voltage of 2 V in S-ED ensures a balance between lithium recovery efficiency, selectivity, and energy consumption. This integration optimizes energy utilization by minimizing the energy consumption in MD and reducing electrical resistance in S-ED, leading to a low SEC of 0.04 kW h per gram Li^+. The energy compatibility between the two processes highlights the potential of this hybrid approach for sustainable and efficient lithium extraction from geothermal brines.

3.6. Long-term stability of ion exchange membranes in S-ED

A long-term stable operation of S-ED is a critical factor for its successful commercial application. Fig. 9 shows the results from the long-term stability tests of the S-ED process for a 24 h

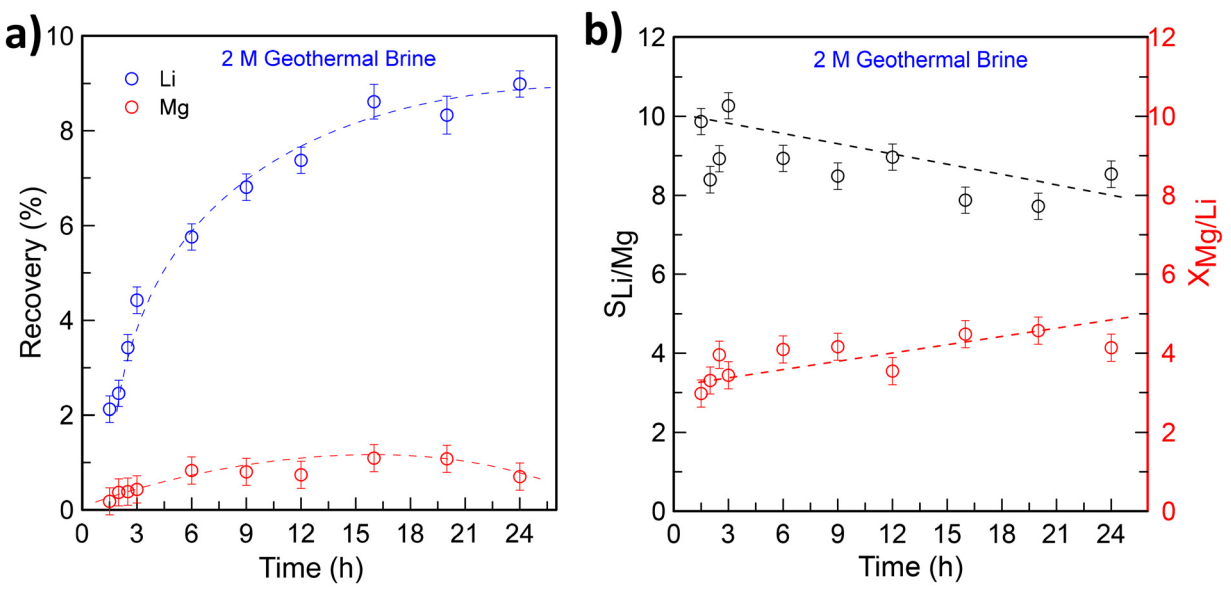

Fig. 9 Long-term performance evaluation of S-ED, showing (a) the recovery rates of Li^+ and Mg^{2+} and (b) the selectivity and Mg/Li ratio in the concentrate stream over 24 h. Experiments were conducted with a 2 M geothermal brine feed under an applied voltage of 2 V to assess membrane stability and separation efficiency.

period performed under the optimal conditions of 2 M geothermal brine and at an applied voltage of 2 V. Lithium recovery exhibits a rapid initial increase (Fig. 9a), indicating efficient ion transport in the early phase. However, the system reaches a plateau after 20 h (at about 8% recovery) which could be associated with the rise of the concentration polarization phenomenon or other mass transfer limiting effects like back-diffusion of ions or electro-osmotic drag that could lead to a near-steady ion recovery rate. In contrast, the Mg recovery remains significantly lower, confirming good membrane selectivity. However, the selectivity was observed to have a slight decrease with time (Fig. 9b) from about 10 to 8, which was accompanied by a gradual increase of the Mg/Li ratio from 3 to 5, suggesting a minor selectivity reduction calling for further improvements, for instance, in terms of using a well-tuned membrane resistant to transport limiting effects.

4. Conclusions

This study presents an innovative approach based on integrated MD and S-ED system for sustainable lithium extraction from geothermal brines, addressing the growing demand for lithium while promoting energy-efficient resource recovery. The MD process effectively concentrated geothermal water, achieving high water recovery rates of up to 97.6% with VRFs of 15.1, 28.1, and 43.1 for feed concentrations of 1 M, 2 M, and 3 M, respectively. By utilizing geothermal heat at 40 °C, the MD stage eliminated external energy requirements, rendering the process energy-neutral and reducing specific thermal energy consumption to zero.

In the S-ED stage, lithium recovery and selectivity were influenced by feed concentration and applied voltage. An optimal voltage of 2 V demonstrated the best performance across various feed concentrations, achieving a specific energy consumption of 0.04 kW h per gram Li^+ and a current efficiency of 4.1% at 2 M. Although higher feed concentration enhances lithium selectivity due to improved Donnan exclusion, it also intensifies ion competition and membrane saturation, which in turn increases energy consumption and reduces current efficiency. Experimental results indicate that selectivity peaks at separation factors of 4.7 and 9.3 for 1 M and 3 M solutions, respectively, before declining at higher voltages due to the increased transport of competing ions. This underscores the necessity of optimizing the trade-off between selectivity and energy efficiency. In particular, precise control of the applied voltage relative to LCD and dynamic current adjustments are essential for mitigating ion competition effects and preventing excessive energy losses.

The synergistic integration of MD and S-ED presents a promising route for efficient and sustainable lithium extraction, though advancements in materials and process integration are crucial for its widespread adoption. Further optimization of the integrated system requires targeted advancements in materials and process development, along with a coordinated approach to managing thermal and electrical energy demands. The development of high-flux, fouling-resistant MD membranes, as well as photothermal enhancements combined with S-ED membranes engineered for enhanced lithium selectivity and reduced electrical resistance, is critical for improving system efficiency. Ion-exchange membranes (IEMs) with increased charge density or lithium-specific functional groups can facilitate selective Li^+ transport while effectively excluding competing cations such as Na^+ and K^+. Energy optimization can be achieved through dynamic current density modulation while refined module design improves flow dynamics and mass transfer, reducing energy losses associated with concentration polarization other relevant effects. This can be assisted by process modeling and optimization strategies for minimizing energy consumption while maximizing lithium recovery.

Data availability

All relevant data are within the manuscript.

Conflicts of interest

The authors declare that they have no known competing financial interests or personal relationships that could have appeared to influence the work reported in this publication.

Acknowledgements

Efrem Curcio, Sergio Santoro, Loredana De Bartolo, Roviel Berhane Zegeye and Alula Selomon Embaye acknowledge the financial support of the European Union's Horizon Europe Research and Innovation Programme under the project EXBRINER "Next-generation membrane technologies for sustainable exploitation of seawater brine resources: transition towards a circular blue industry" (HORIZON-MSCA-DN-2021, Grant Agreement No. 101072449). Efrem Curcio and Pietro Argurio acknowledge the financial support of Next Generation EU – Italian NRRP, Mission 4, Component 2, Investment 1.5, call for the creation and strengthening of 'Innovation Ecosystems', building 'Territorial R&D Leaders' (Directorial Decree n. 2021/3277) – project Tech4You – Technologies for climate change adaptation and quality of life improvement, n. ECS0000009.

References

1 W. A. Hart, O. Beumel and T. P. Whaley, *The chemistry of lithium, sodium, potassium, rubidium, cesium and francium: pergamon texts in inorganic chemistry*, Elsevier, 2013.
2 S. Gu, J. Kong, L. Xing, H. Sun, Y. Qiu and J. Yu, *J. Environ. Chem. Eng.*, 2022, **10**, 107745.
3 L. Xing, S. Lin and J. Yu, *Ind. Eng. Chem. Res.*, 2021, **60**, 10303–10311.

4 L. Xing, J. Bao, S. Zhou, Y. Qiu, H. Sun, S. Gu and J. Yu, *Chem. Eng. J.*, 2021, **420**, 129593.
5 V. P. Parikh, A. Ahmadi, M. H. Parekh, F. Sadeghi and V. G. Pol, *Environ. Sci. Technol.*, 2019, **53**, 3757–3763.
6 B. Diouf and R. Pode, *Renewable Energy*, 2015, **76**, 375–380.
7 H. Vikström, S. Davidsson and M. Höök, *Appl. Energy*, 2013, **110**, 252–266.
8 L. A. Munk, S. A. Hynek, D. C. Bradley, D. Boutt, K. Labay and H. Jochens, Lithium Brines: A Global Perspective, in *Rare Earth and Critical Elements in Ore Deposits*, Society of Economic Geologists, 2016, vol. 18, pp. 339–365.
9 S. E. Kesler, P. W. Gruber, P. A. Medina, G. A. Keoleian, M. P. Everson and T. J. Wallington, *Ore Geol. Rev.*, 2012, **48**, 55–69.
10 A. González, C. Sanhueza and C. Roa, *Government of Chile, Comisión Chilena del Cobre, Presentation*, 2020, pp. 26.
11 V. Petrova, *Eurasian Proc. Sci. Technol. Eng. Math.*, 2023, **26**, 664–671.
12 P. Kowalski and C. Legendre, *Raw materials critical for the green transition: Production, international trade and export restrictions*, Organisation for Economic Cooperation and Development (OECD), 2023, DOI: **10.1787/c6bb598b-en**.
13 M. L. Vera, W. R. Torres, C. I. Galli, A. Chagnes and V. Flexer, *Nat. Rev. Earth Environ.*, 2023, **4**, 149–165.
14 R. A. Tufa, *Environ. Technol. Innov.*, 2015, **4**, 182–193.
15 A. Razmjou, M. Asadnia, E. Hosseini, A. Habibnejad Korayem and V. Chen, *Nat. Commun.*, 2019, **10**, 5793.
16 C. B. Tabelin, J. Dallas, S. Casanova, T. Pelech, G. Bournival, S. Saydam and I. Canbulat, *Miner. Eng.*, 2021, **163**, 106743.
17 L. Gregoir and K. van Acker, *Eurometaux*, KU Leuven, 2022.
18 W. T. Stringfellow and P. F. Dobson, *Energies*, 2021, **14**, 6805.
19 I. Warren, *Techno-economic analysis of lithium extraction from geothermal brines*, National Renewable Energy Lab. (NREL), Golden, CO, United States, 2021.
20 P. Bayer, L. Rybach, P. Blum and R. Brauchler, *Renewable Sustainable Energy Rev.*, 2013, **26**, 446–463.
21 J. Bundschuh and B. Tomaszewska, *Geothermal water management*, CRC Press, 2018.
22 B. Tomaszewska and A. Szczepański, *Environ. Sci. Pollut. Res.*, 2014, **21**, 11409–11417.
23 A. Kumar, H. Fukuda, T. A. Hatton and J. H. Lienhard, *ACS Energy Lett.*, 2019, **4**, 1471–1474.
24 R. J. Bowell, L. Lagos, C. R. de los Hoyos and J. Declercq, *Elements*, 2020, **16**, 259–264.
25 E. J. Dugamin, A. Richard, M. Cathelineau, M.-C. Boiron, F. Despinois and A. Brisset, *Sci. Rep.*, 2021, **11**, 21091.
26 A.-L. Toba, R. T. Nguyen, C. Cole, G. Neupane and M. P. Paranthaman, *Resour., Conserv. Recycl.*, 2021, **169**, 105514.
27 B. Sanjuan, B. Gourcerol, R. Millot, D. Rettenmaier, E. Jeandel and A. Rombaut, *Geothermics*, 2022, **101**, 102385.
28 E. Knapik, G. Rotko and M. Marszałek, *Energies*, 2023, **16**, 6628.
29 A. Siekierka, B. Tomaszewska and M. Bryjak, *Desalination*, 2018, **436**, 8–14.
30 S. Sutijan, S. A. Darma, C. M. Hananto, V. S. H. Sujoto, F. Anggara, S. N. A. Jenie, W. Astuti, F. R. Mufakhir, S. Virdian and A. P. Utama, *Membranes*, 2023, **13**, 86.
31 S. Chen, Z. Chen, Z. Wei, J. Hu, Y. Guo and T. Deng, *Chem. Eng. J.*, 2021, **410**, 128320.
32 J. Miao, K. Zhao, F. Guo, L. Xu, Y. Xie and T. Deng, *Desalination*, 2022, **527**, 115570.
33 L. Talens Peiró, G. Villalba Méndez and R. U. Ayres, *JOM*, 2013, **65**, 986–996.
34 B. K. Pramanik, M. B. Asif, S. Kentish, L. D. Nghiem and F. I. Hai, *J. Environ. Chem. Eng.*, 2019, **7**, 103395.
35 R. A. Tufa, Y. Noviello, G. Di Profio, F. Macedonio, A. Ali, E. Drioli, E. Fontananova, K. Bouzek and E. Curcio, *Appl. Energy*, 2019, **253**, 113551.
36 V. R. Moreira, Y. A. R. Lebron and M. C. S. Amaral, *Chem. Eng. J.*, 2022, **430**, 133006.
37 G. Di Profio, E. Curcio and E. Drioli, *Ind. Eng. Chem. Res.*, 2010, **49**, 11878–11889.
38 M. M. A. Shirazi, A. Ali and C. A. Quist-Jensen, *Desalination*, 2024, **571**, 117109.
39 A. Cerda, M. Quilaqueo, L. Barros, G. Seriche, M. Gim-Krumm, S. Santoro, A. H. Avci, J. Romero, E. Curcio and H. Estay, *J. Water Process Eng.*, 2021, **41**, 102063.
40 S. Santoro, A. H. Avci, A. Politano and E. Curcio, *Chem. Soc. Rev.*, 2022, **51**, 6087–6125.
41 A. H. Avci, S. Santoro, A. Politano, M. Propato, M. Micieli, M. Aquino, Z. Wenjuan and E. Curcio, *Chem. Eng. Process.*, 2021, **164**, 108382.
42 S. Santoro, M. Aquino, C. Rizza, J. Occhiuzzi, D. Mastrippolito, G. D'Olimpio, A. H. Avci, J. De Santis, V. Paolucci and L. Ottaviano, *Desalination*, 2023, **546**, 116186.
43 R. Wang and S. Lin, *Environ. Sci. Technol.*, 2024, **58**, 3552–3563.
44 X.-Y. Nie, S.-Y. Sun, Z. Sun, X. Song and J.-G. Yu, *Desalination*, 2017, **403**, 128–135.
45 X.-Y. Nie, S.-Y. Sun, X. Song and J.-G. Yu, *J. Membr. Sci.*, 2017, **530**, 185–191.
46 W. Wang, G. Hong, Y. Zhang, X. Yang, N. Hu, J. Zhang, P. Sorokin and L. Shao, *J. Membr. Sci.*, 2023, **675**, 121534.
47 W. Wang, C. Wang, R. Huang, G. Hong, Y. Zhang, X. Zhang and L. Shao, *Water Res.*, 2024, 122729.
48 F. Macedonio, E. Curcio and E. Drioli, *Desalination*, 2007, **203**, 260–276.
49 J. L. Prante, J. A. Ruskowitz, A. E. Childress and A. Achilli, *Appl. Energy*, 2014, **120**, 104–114.
50 A. Politano, R. A. Al-Juboori, S. Alnajdi, A. Alsaati, A. Athanassiou, M. Bar-Sadan, A. N. Beni, D. Campi, A. Cupolillo and G. D'Olimpio, *J. Phys.: Energy*, 2024, **6**, 021502.
51 G. Vespasiano, PhD Thesis, University of Calabria, 2015, pp. 213 (In Italian).
52 D. L. Ball and D. A. Boateng, *US pat.*, 4636295A, 1987.
53 X. Wen, P. Ma, C. Zhu, Q. He and X. Deng, *Sep. Purif. Technol.*, 2006, **49**, 230–236.

54 Y. Gang, S. Hong, L. Wenqiang, X. Weihong and X. U. Nanping, *Chin. J. Chem. Eng.*, 2011, **19**, 586–591.
55 M. Al-Furaiji, J. T. Arena, J. Ren, N. Benes, A. Nijmeijer and J. R. McCutcheon, *Membranes*, 2019, **9**, 60.
56 S. Santoro, M. Aquino, C. Rizza, A. Cupolillo, D. W. Boukhvalov, G. D'Olimpio, S. Abramovich, A. Agarwal, M. B. Sadan and A. Politano, *Desalination*, 2023, **563**, 116730.
57 M. Quilaqueo, G. Seriche, L. Barros, C. González, J. Romero, R. Ruby-Figueroa, S. Santoro, E. Curcio and H. Estay, *Desalination*, 2022, **537**, 115887.
58 F. Russo, S. Santoro, F. Galiano, C. Ursino, E. Avruscio, E. Di Nicolò, G. Desiderio, G. Lombardo, A. Criscuoli and A. Figoli, *J. Membr. Sci.*, 2023, **685**, 121928.
59 A. Ali, F. Macedonio, E. Drioli, S. Aljlil and O. A. Alharbi, *Chem. Eng. Res. Des.*, 2013, **91**, 1966–1977.
60 A. Anvari, A. A. Yancheshme, K. M. Kekre and A. Ronen, *J. Membr. Sci.*, 2020, **616**, 118413.
61 A. Ali, M. M. A. Shirazi, L. Nthunya, R. Castro-Muñoz, N. Ismail, N. Tavajohi, G. Zaragoza and C. A. Quist-Jensen, *Desalination*, 2024, **581**, 117584.
62 S. Shalaby, A. Kabeel, H. Abosheiasha, M. Elfakharany, E. El-Bialy, A. Shama and R. D. Vidic, *J. Cleaner Prod.*, 2022, **366**, 132949.
63 S. Santoro, M. Aquino, D. H. Seo, T. Van Der Laan, M. Lee, J. S. Yun, M. J. Park, A. Bendavid, H. K. Shon and A. H. Avci, *J. Colloid Interface Sci.*, 2022, **623**, 607–616.
64 E. Drioli, E. Curcio, A. Criscuoli and G. D. Profio, *J. Membr. Sci.*, 2004, **239**, 27–38.
65 R. Molinari, A. H. Avci, P. Argurio, E. Curcio, S. Meca, M. Plà-Castellana and J. L. Cortina, *J. Cleaner Prod.*, 2021, **328**, 129645.
66 M. La Cerva, L. Gurreri, M. Tedesco, A. Cipollina, M. Ciofalo, A. Tamburini and G. Micale, *Desalination*, 2018, **445**, 138–148.
67 A. Nakayama, Y. Sano, X. Bai and K. Tado, *Desalination*, 2017, **404**, 41–49.
68 V. V. Nikonenko, A. V. Kovalenko, M. K. Urtenov, N. D. Pismenskaya, J. Han, P. Sistat and G. Pourcelly, *Desalination*, 2014, **342**, 85–106.
69 S. Pawlowski, P. Sistat, J. G. Crespo and S. Velizarov, *J. Membr. Sci.*, 2014, **471**, 72–83.
70 A. Doyen, C. Roblet, A. L'Archevêque-Gaudet and L. Bazinet, *J. Membr. Sci.*, 2014, **452**, 453–459.
71 K. Tado, F. Sakai, Y. Sano and A. Nakayama, *Desalination*, 2016, **378**, 60–66.
72 A. Campione, L. Gurreri, M. Ciofalo, G. Micale, A. Tamburini and A. Cipollina, *Desalination*, 2018, **434**, 121–160.
73 H.-W. Rösler, F. Maletzki and E. Staude, *J. Membr. Sci.*, 1992, **72**, 171–179.
74 M. Isaacson and A. A. Sonin, *Ind. Eng. Chem. Process Des. Dev.*, 1976, **15**, 313–321.
75 A. M. Benneker, J. Klomp, R. G. Lammertink and J. A. Wood, *Desalination*, 2018, **443**, 62–69.
76 C. Mahendra, P. S. Sai and C. A. Babu, *Desalination*, 2014, **353**, 8–14.
77 K. J. Min, J. H. Kim and K. Y. Park, *Sci. Total Environ.*, 2021, **757**, 143762.
78 S. Xutoi and C. Guang, *Desalination*, 1983, **46**, 263–274.
79 Z.-y. Ji, Q.-b. Chen, J.-s. Yuan, J. Liu, Y.-y. Zhao and W.-x. Feng, *Sep. Purif. Technol.*, 2017, **172**, 168–177.
80 P.-Y. Ji, Z.-Y. Ji, Q.-B. Chen, J. Liu, Y.-Y. Zhao, S.-Z. Wang, F. Li and J.-S. Yuan, *Sep. Purif. Technol.*, 2018, **207**, 1–11.
81 S. Bunani, M. Arda, N. Kabay, K. Yoshizuka and S. Nishihama, *Desalination*, 2017, **416**, 10–15.
82 J. Yoon, V. Q. Do, V.-S. Pham and J. Han, *Water Res.*, 2019, **159**, 501–510.
83 K. M. Chehayeb, D. M. Farhat and K. G. Nayar, *Desalination*, 2017, **420**, 167–182.
84 J. Yoon, M. T. Flavin and J. Han, *Water Res.*, 2021, **201**, 117351.
85 S. Moshtarikhah, N. Oppers, M. De Groot, J. Keurentjes, J. Schouten and J. Van Der Schaaf, *J. Appl. Electrochem.*, 2017, **47**, 51–62.
86 J. Ying, M. Luo, Y. Jin and J. Yu, *Desalination*, 2020, **492**, 114621.
87 A. Volkov, S. Paula and D. Deamer, *Bioelectrochem. Bioenerg.*, 1997, **42**, 153–160.
88 G. Liu, Z. Zhao and L. He, *Desalination*, 2020, **474**, 114185.
89 X.-C. Zhang, J. Wang, Z.-Y. Ji, P.-Y. Ji, J. Liu, Y.-Y. Zhao, F. Li and J.-S. Yuan, *J. Environ. Chem. Eng.*, 2021, **9**, 106635.
90 Z. Zhao, G. Liu, H. Jia and L. He, *J. Membr. Sci.*, 2020, **596**, 117685.
91 H. Strathmann, *Desalination*, 2010, **264**, 268–288.
92 M. Ben Sik Ali, A. Mnif, B. Hamrouni and M. Dhahbi, *Ionics*, 2010, **16**, 621–629.
93 M. Sadrzadeh and T. Mohammadi, *Desalination*, 2008, **221**, 440–447.
94 J. Ying, Y. Lin, Y. Zhang and J. Yu, *ACS ES&T Water*, 2023, **3**, 1720–1739.
95 Q.-B. Chen, Z.-Y. Ji, J. Liu, Y.-Y. Zhao, S.-Z. Wang and J.-S. Yuan, *J. Membr. Sci.*, 2018, **548**, 408–420.
96 T. Luo, S. Abdu and M. Wessling, *J. Membr. Sci.*, 2018, **555**, 429–454.
97 R. Abu-Rjal, V. Chinaryan, M. Z. Bazant, I. Rubinstein and B. Zaltzman, *Phys. Rev. E: Stat., Nonlinear, Soft Matter Phys.*, 2014, **89**, 012302.
98 T. Dong, J. Yao, Y. Wang, T. Luo and L. Han, *Desalination*, 2020, **488**, 114521.
99 H. Strathmann, *Ion-exchange membrane separation processes*, Elsevier, 2004.
100 H. Fan, Y. Huang, I. H. Billinge, S. M. Bannon, G. M. Geise and N. Y. Yip, *ACS ES&T Eng.*, 2022, **2**, 1274–1286.
101 I. Abdulazeez, B. Salhi, N. Baig and Q. Peng, *Membranes*, 2021, **11**, 940.
102 J. Meng, X. Shi, S. Wang, Z. Hu, D. Y. Koseoglu-Imer, P. N. Lens and X. Zhan, *J. Water Process Eng.*, 2024, **65**, 105855.
103 R. Mohammadi, D. L. Ramasamy and M. Sillanpää, *Desalination*, 2021, **498**, 114726.

104 N. Parsa, A. Moheb, A. Mehrabani-Zeinabad and M. A. Masigol, *Chem. Eng. Res. Des.*, 2015, **98**, 81–88.
105 Z. H. Foo, J. B. Thomas, S. M. Heath, J. A. Garcia and J. H. Lienhard, *Environ. Sci. Technol.*, 2023, **57**, 14747–14759.
106 Z.-Y. Guo, Z.-Y. Ji, Q.-B. Chen, J. Liu, Y.-Y. Zhao, F. Li, Z.-Y. Liu and J.-S. Yuan, *J. Cleaner Prod.*, 2018, **193**, 338–350.
107 M. Shi, L. A. Diaz, J. R. Klaehn, A. D. Wilson and T. E. Lister, *ACS Sustainable Chem. Eng.*, 2022, **10**, 11773–11781.
108 Z. Xing and M. Srinivasan, *Chem. Eng. J.*, 2023, **474**, 145306.
109 P. P. Sharma, V. Yadav, A. Rajput, H. Gupta, H. Saravaia and V. Kulshrestha, *Desalination*, 2020, **496**, 114755.
110 F. Rögener and L. Tetampel, *Membranes*, 2022, **12**, 1142.
111 B. Mojtahedi, M. Askari and A. Dolati, *ACS Sustainable Chem. Eng.*, 2025, **13**, 3107–3118.
112 Y. Zhao, W. Shi, B. Van der Bruggen, C. Gao and J. Shen, *Adv. Mater. Interfaces*, 2018, **5**, 1701449.
113 S. Melnikov, N. Sheldeshov, V. Zabolotsky, S. Loza and A. Achoh, *Sep. Purif. Technol.*, 2017, **189**, 74–81.